Ambient- to Elevated-Temperature Fracture and Fatigue Properties of Mo-Si-B Alloys: Role of Microstructure

J.J. KRUZIC, J.H. SCHNEIBEL, and R.O. RITCHIE

Ambient- to elevated-temperature fracture and fatigue-crack growth results are presented for five Mo-Mo_3Si-Mo_5SiB_2–containing α-Mo matrix (17 to 49 vol pct) alloys, which are compared to results for intermetallic-matrix alloys with similar compositions. By increasing the α-Mo volume fraction, ductility, or microstructural coarseness, or by using a continuous α-Mo matrix, it was found that improved fracture and fatigue properties are achieved by promoting the active toughening mechanisms, specifically crack trapping and crack bridging by the α-Mo phase. Crack-initiation fracture toughness values increased from 5 to 12 MPa$\sqrt{m}$ with increasing α-Mo content from 17 to 49 vol pct, and fracture toughness values rose with crack extension, ranging from 8.5 to 21 MPa$\sqrt{m}$ at ambient temperatures. Fatigue thresholds benefited similarly from more α-Mo phase, and the fracture and fatigue resistance was improved for all alloys tested at 1300 °C, the latter effects being attributed to improved ductility of the α-Mo phase at elevated temperatures.

I. INTRODUCTION

A major limitation in the technological advancement of aerospace engines and power generation is the lack of higher-temperature structural materials to replace conventional nickel-base superalloys. Indeed, single-crystal nickel-base superalloys have essentially reached their temperature limit and are unsuitable for structural use above ~1100 °C.[1] Unfortunately, using higher melting-point (>2000 °C) materials presents several obstacles as adequate fracture, fatigue, oxidation, and creep resistance must be maintained. For example, materials based on refractory metals such as molybdenum typically suffer from poor oxidation and creep resistance. While the formation of molybdenum silicides and borosilicides significantly improves these properties,[2,3,4] such intermetallic compounds are invariably brittle and provide little resistance to fracture.

To meet the need of developing useful structural molybdenum-based alloys, two distinct multiphase Mo-Si-B alloy systems have been proposed, based on the phases: (1) Mo_3Si, Mo_5SiB_2 (T2), and Mo_5Si_3 (T1), by Akinc and co-workers;[2–5] and (2) α-Mo, Mo_3Si, and Mo_5SiB_2 (T2), by Berczik.[6,7] With regard to fracture resistance, the latter alloys hold more promise since they contain the relatively ductile α-Mo phase, with Si and B in solid solution, in addition to the brittle intermetallic phases Mo_3Si and Mo_5SiB_2.

The microstructural arrangement of these phases is critical in determining the properties. Indeed, while alloys containing molybdenum particles surrounded by the hard but brittle intermetallic phases display definitive improvements in toughness compared to monolithic silicides,[8,9] larger improvements in fracture and fatigue resistance have been achieved using a continuous α-Mo matrix.[10] Although these α-Mo matrix alloys resemble nickel-base (γ/γ') superalloys in their similarly high volume fraction of intermetallic phase, an additional difficulty for Mo-Si-B materials is that, unlike the γ' Ni_3Al phase, Mo_3Si and Mo_5SiB_2 exhibit essentially no ductility at ambient temperatures. These factors suggest that making the most effective use of the relatively ductile molybdenum phase is important for achieving high fracture and fatigue resistance. However, since the development of serviceable Mo-Si-B alloys will depend on compromises between several material properties,[11] there is a need to understand more specifically how different microstructural parameters affect the fracture and fatigue behavior. Accordingly, it is the objective of this work to present results on the fracture toughness and fatigue-crack propagation properties at ambient to elevated (1300 °C) temperatures for a series of five Mo-Si-B alloys with continuous α-Mo matrices; such results are compared to those for intermetallic-matrix alloys with similar compositions[8,9,11] in an effort to understand the specific role of microstructure in influencing the salient micromechanisms responsible for their fracture and fatigue behavior.

II. MATERIALS AND PROCEDURES

To generate microstructures with a continuous α-Mo phase, powders were ground from arc-cast ingots with the composition Mo-20Si-10B at. pct (Mo_3Si-Mo_5SiB_2) and vacuum annealed to remove silicon from the surface and to leave an α-Mo coating on each particle.[12] The surface-modified powders were then hot-isostatically pressed in evacuated Nb cans for 4 hours at 1600 °C at 200 MPa pressure. Five alloys were produced differing in volume fraction of the α-Mo matrix and coarseness of the intermetallic particles. Polished metallurgical sections were used to characterize the microstructures and to determine the α-Mo content of each alloy. These alloys contained Mo_3Si (cubic A15 structure) and Mo_5SiB_2 (tetragonal $D8_1$ structure) intermetallic phases within a continuous α-Mo matrix; two alloys

J.J. KRUZIC, Assistant Professor, is with the Department of Mechanical Engineering, Oregon State University, Corvallis, OR 97331. Contact e-mail: jamie.kruzic@oregonstate.edu J.H. SCHNEIBEL, Senior Research Staff Member, is with Oak Ridge National Laboratory, Metals and Ceramics Division, Oak Ridge, TN 37831. R.O. RITCHIE, Professor, is with the Materials Sciences Division, Lawrence Berkeley National Laboratory, and the Department of Materials Science and Engineering, University of California, Berkeley, CA 94720.

Manuscript submitted January 3, 2005.

designated* as F34 and M34 had 34 vol pct α-Mo with initial powder sizes of $\leq$45 and 45 to 90 μm, respectively, while three coarse microstructured alloys had 17, 46, and 49 vol pct α-Mo (designated C17, C46, and C49, respectively) and an initial powder size of 90 to 180 μm (Figure 1). Note that alloys F34, M34, and C49 correspond to the alloys designated "fine," "medium," and "coarse" in Reference 10, where initial fracture and fatigue data were presented. In addition to the equilibrium Mo_3Si and Mo_5SiB_2 phases, small amounts of the nonequilibrium Mo_2B phase were detected by X-ray diffraction.

The chemical compositions were different from the initial starting powders due to the vacuum annealing process. Final alloy compositions were determined by a combination of inductively coupled-plasma spectroscopy and combustion-infrared absorption; the latter technique was used to determine the oxygen, carbon, and sulfur content.

Resistance-curve (R-curve) fracture-toughness experiments were performed on disk-shaped, compact-tension DC(T) specimens (14-mm width; 3-mm thickness) in general accordance with ASTM Standard E561.[13] Specimens were precracked by fatigue loading (fatigue conditions described subsequently) half-chevron notched specimens at room temperature until precracks had propagated beyond the half-chevron notch region (which was ~300 to 600 μm in length). Samples were then loaded monotonically in displacement control at ~1 μm/min until the onset of crack extension. At 25 °C, periodic unloads (~10 to 20 pct of peak load) were performed to measure the unloading back-face strain compliance, which was used to determine the crack length.[14] Elevated temperature tests at 1300 °C were conducted in a gettered argon environment using (direct-current) electrical

*The alloy designations constitute a letter followed by a number. The letter refers to the relative coarseness of the microstructure (F = fine, M = medium, and C = coarse); the number refers to the volume percent of the α-Mo phase. Fine, medium, and coarse correspond to $\leq$45, 45 to 90 μm, and 90 to 180 μm starting powders, respectively.

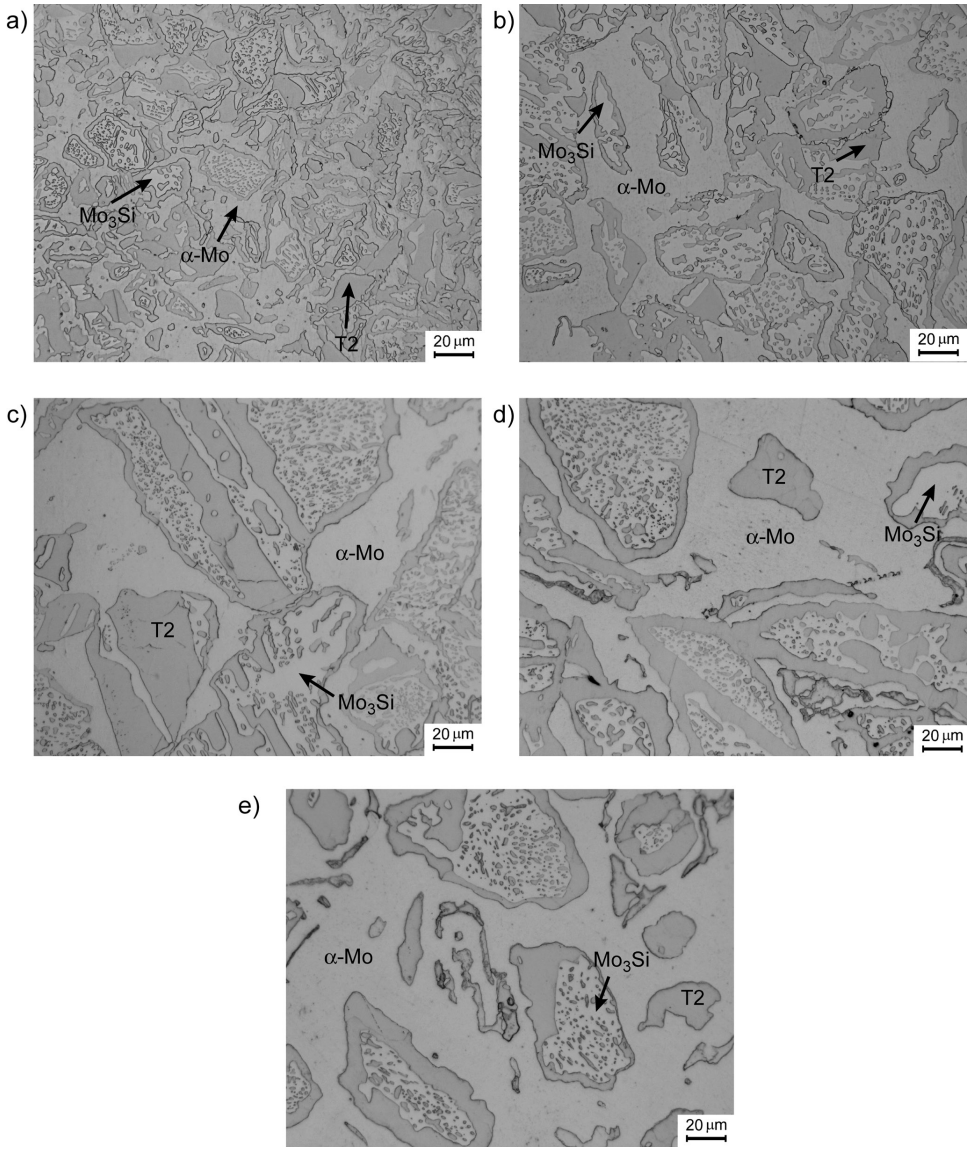

Fig. 1—Optical micrographs of the (*a*) F34, (*b*) M34, (*c*) C17, (*d*) C46, and (*e*) C49 alloys, showing continuous α-Mo matrices with Mo_3Si and T2 (etched with Murakami's reagent).

potential-drop techniques to monitor crack length. Such ultrahigh temperature testing is complex to perform; full details of our procedures are described in Reference 15. At both 25 and 1300 °C, fracture resistance was assessed as a function of crack length based on the loads associated with each crack length determined by the compliance or electric potential methods. In specific instances, testing was paused to observe crack profiles such that interactions of the crack with microstructural features could be documented using optical microscopy and scanning electron microscopy (SEM). The R-curve tests were continued until catastrophic failure of the specimens occurred or more than at least 3 mm of crack extension was achieved, at which point the test was concluded. For cases where tests were interrupted or catastrophic failure did not occur, crack lengths determined by compliance or electrical potential methods were verified using optical measurements. Since both compliance and potential-drop techniques can be prone to errors due to crack bridging between the crack faces, any discrepancies in crack length were accounted for by assuming that they accumulated linearly with crack extension.

Fatigue-crack growth testing (25 Hz, sinusoidal waveform) was performed at 25 and 1300 °C in identical environments to R-curve testing in general accordance with ASTM standard E647[16] using computer-controlled servohydraulic testing machines at a load ratio R (ratio of minimum to maximum loads) of 0.1. Crack-growth rates, da/dN, were determined as a function of the stress-intensity range, ΔK, using continuous load shedding to maintain a ΔK gradient ($=[1/\Delta K]d\Delta K/da$) of $\pm 0.08\ \mathrm{mm}^{-1}$, corresponding to increasing or decreasing ΔK conditions, respectively. The ΔK_{TH} fatigue thresholds, operationally defined at a minimum growth rate of 10^{-10} to 10^{-11} m/cycle, were approached under decreasing ΔK conditions. Testing was again periodically interrupted to conduct optical microscopy and SEM such that any errors in crack-length measurement could be accounted for, as described previously. Characterization of the fatigue and fracture surfaces was performed using SEM after specimen failure.

III. RESULTS

A. *Alloy Compositions*

Final compositions of the alloys are shown in Table I. As expected, the alloys with the highest α-Mo content had the lowest Si concentration, as a result of the vacuum annealing process. Unexpectedly, the relatively low B concentrations for alloys C46 and C49 suggest that not only Si, but also B, was partially removed during the vacuum annealing step. Nearly identical concentrations of Mo, Si, and B were found for alloys F34 and M34, reflective of their nearly identical α-Mo volume fractions. Alloys C46 and C49, however, had quite dissimilar measured compositions despite similar α-Mo volume fractions; the reasons for this are not clear. Using the chemical composition data from Table I and the equilibrium 1600 °C Mo-Si-B ternary phase diagram,[17] estimates of the phase volume fractions were made based on the lattice parameters for pure Mo and stoichiometric Mo_3Si and Mo_5SiB_2 (Table II). Despite the simplifying assumptions and the fact that nonequilibrium MoB_2 was ignored, there was relatively good agreement between the estimates and the α-Mo volume fractions measured from micrographs for all alloys except C49, suggesting that the chemical analysis for alloy C49 may be in error.

Table I. Compositions of Mo-Si-B Alloys (Atomic Percent)

Element	F34	M34	C17	C46	C49
Mo	76.68	77.28	73.62	80.47	85.14
Si	11.32	11.32	15.02	9.46	6.68
B	11.42	10.92	10.99	9.89	8.05
Al	0.32	0.26	0.17	0.12	0.09
Fe	0.11	0.01	0.08	0.04	0.03
Ni	—	0.13	—	—	—
O	0.08	0.005	0.05	0.01	0.01
C	0.07	0.07	0.06	<0.07	<0.07
S	0.005	0.007	0.007	0.005	0.005

B. *Fracture Toughness*

Room-temperature R-curves for the five Mo-Mo_3Si-T2 alloys plotted in terms of the stress intensity, K, clearly indicate rising fracture toughness with crack extension (Figure 2(a)). The measured R-curves are mostly linear, although the catastrophic failure of some samples suggests a sharp flattening out of the R-curves, which was not measured. The R-curve toughening effects were most significant for the coarse alloys C46 and C49, which had peak room-temperature toughnesses in excess of 20 MPa$\sqrt{\mathrm{m}}$, *i.e.*, up to 7 times higher than that of monolithic molybdenum silicides ($MoSi_2$, Mo_3Si), which have toughnesses of 3 to 4 MPa$\sqrt{\mathrm{m}}$.[18,19] The current alloys are also tougher than Mo-Si-B alloys with discontinuous α-Mo phase (22 to 38 vol pct), which displayed modest R-curve behavior with much lower peak toughness (~4.0 to 7.5 MPa$\sqrt{\mathrm{m}}$).[8,9]

Additionally, experiments at 1300 °C on alloys M34, C17, and C46 indicated that the fracture toughness improves at higher temperatures. The R-curve data at 1300 °C are shown in Figure 2(b), along with room-temperature data for comparison. Increasing the temperature had a particularly significant effect on the crack-initiation toughness, K_i, which defines the start of the R-curve; specifically, K_i values for alloys M34 and C17 were, respectively, 63 and 65 pct higher at 1300 °C than at 25 °C. Again, the toughness properties were most impressive for the coarse, high α-Mo alloy C46, which experienced toughening at 1300 °C to such a degree that large-scale crack blunting and deformation occurred and linear-elastic fracture mechanics (LEFM) was no longer a valid method for assessing the toughness using the present specimen size. Figure 3(a) illustrates this behavior; indeed, a deformation zone greater than 1.5 mm in size may be seen, which is on the order of sample dimensions and violates the small-scale yielding requirements for LEFM. Crack blunting was also observed, to a much smaller degree, in the other alloys tested at 1300 °C, as seen in Figure 3(b) for alloy M34.

Table II. Estimated Volume Percent of Each Phase Based on Compositions in Table I

Phase	F34	M34	C17	C46	C49
α-Mo	37.5	37.5	18.3	49.1	66.5*
Mo_3Si	21.9	21.9	40.3	14.6	4.7
Mo_5SiB_2	40.6	40.6	41.4	36.3	28.8

*Inconsistent with measured α-Mo phase volume fraction.

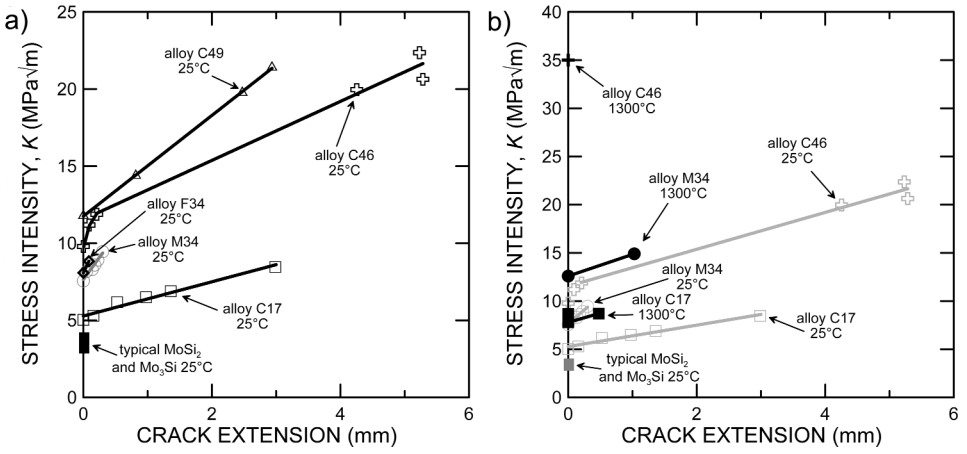

Fig. 2—R-curves showing the fracture resistance of the continuous α-Mo matrix Mo-Si-B alloys at (*a*) room temperature (open symbols) and (*b*) 1300 °C (closed symbols). Also shown are previously reported room-temperature values for unreinforced molybdenum silicides.[18,19]

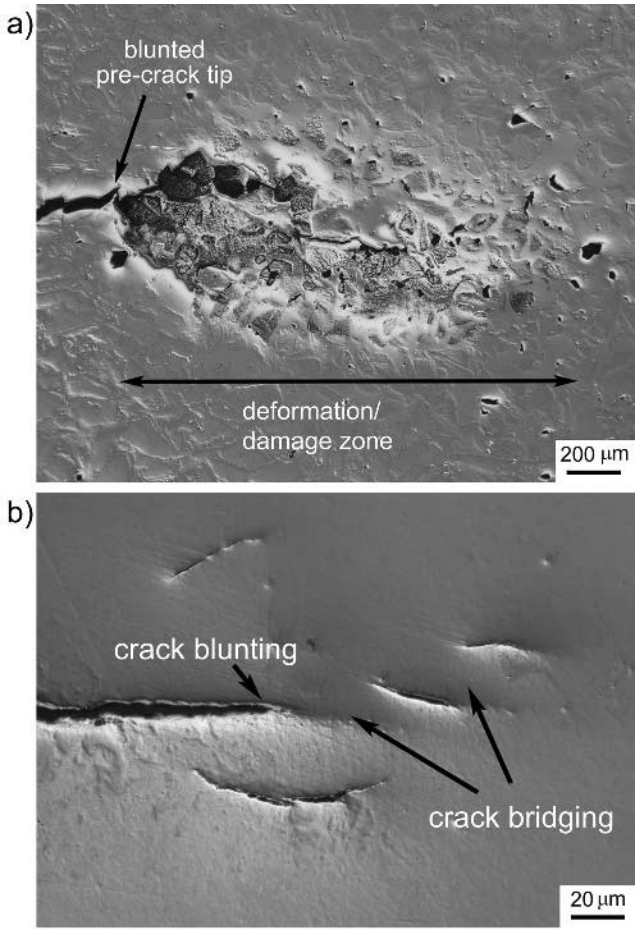

Fig. 3—Optical micrographs illustrating the crack blunting and damage zone ahead of the crack tips after R-curve testing at 1300 °C for alloys (*a*) C46 and (*b*) M34. Notice the order of magnitude difference in scale between the two photos. Furthermore, crack bridging is seen for alloy M34 in (b). Nomarski differential image contrast was used for both images, and the nominal crack growth direction was left to right.

For alloy C46, the *J*-integral may be estimated based on the measured crack-tip opening displacement, δ, by the relation[20]

$$J = d_n \sigma_0 \delta \qquad [1]$$

where σ_0 is the yield strength, and d_n is a dimensionless factor that varies between 0.3 and 1 depending upon the yield strain, strain-hardening coefficient, and stress state. Limited tensile tests at 1200 °C on alloy C49, which is similar in microstructure and composition to alloy C46, gave yield and ultimate tensile strengths of 336 and 354 MPa, respectively.[10] Thus, using $d_n = 1$, which reflects a plane-stress condition with minimal strain hardening,[20] a yield strength of $\sigma_0 =$ 336 MPa, and the measured δ of 10 μm, gives an estimate of the crack-initiation toughness of $J_i \approx 3360$ J/m^2. When linear-elastic conditions prevail, such a *J* value can be related to the stress intensity, *K*, under mode I conditions by

$$K = \sqrt{JE} \qquad [2]$$

where *E* is the elastic modulus. This allows an estimate of the plane-stress initiation toughness in terms of *K*, which should reflect the value that would have been measured if it were possible to use a larger specimen size to maintain small-scale yielding conditions. From Eq.[2], a plane-stress initiation toughness of $K_i \approx 35$ MPa$\sqrt{\text{m}}$ was deduced using a modulus $E = 360$ GPa, which is based on a simple rule of mixtures using the volume fraction of the α-Mo phase ($E =$ 325 GPa[21]) and the intermetallic phases ($E \approx 390$ GPa[22,23]). The measured or deduced initiation toughness values for each alloy are tabulated in Table III.

C. *Fatigue-Crack Growth*

Fatigue-crack growth results for the five alloys are shown in Figure 4, and may be characterized in terms of a classical power-law relationship:

$$da/dN = C\Delta K^m \qquad [3]$$

It is apparent that at 25 °C, the power-law exponents, *m*, are extremely high, exceeding 78 for all alloys (Table III), which is characteristic of brittle materials such as ceramics. Fatigue-crack growth data are also shown for alloys M34 and C49 at 1300 °C. Although alloy M34 had a similarly high ΔK dependence, the coarse, high α-Mo alloy C49 displayed a transition to more ductile fatigue behavior at 1300 °C, with more than an order of magnitude decrease in the power-law exponent from 78 to 4. An exponent of 4 is similar to what

Table III. Fracture and Fatigue Properties of Mo-Si-B Alloys with α-Mo Matrix

Alloy	Initiation Toughness, K_i, at 25 °C (MPa$\sqrt{m}$)	Initiation Toughness, K_i, at 1300 °C (MPa$\sqrt{m}$)	Fatigue Threshold, $K_{max,TH}$, at 25 °C (MPa$\sqrt{m}$)	Power-Law Exponent, m, at 25 °C
F34	8.0	NA	6.8	125
M34	7.5	12.6	7.2	87
C17	5.0	8.3	5.6	152
C46	9.8	35*	9.9	88
C49	12.0	NA	10.6	78

*Plane stress value estimated from measured crack tip opening displacement (CTOD).

NA—not applicable.

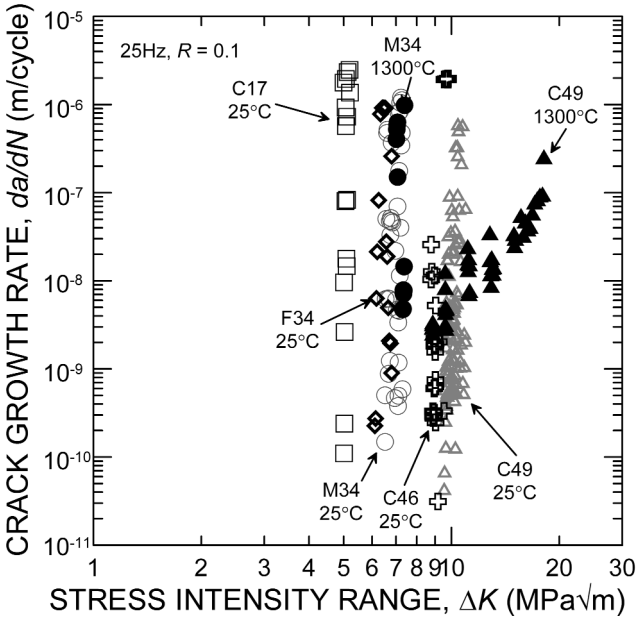

Fig. 4—Fatigue-crack growth rate, *da/dN*, data plotted as a function of applied stress intensity range, ΔK, for continuous α-Mo matrix Mo-Si-B alloys at room (25 °C) and elevated (1300 °C) temperatures. The fatigue threshold clearly increases with increasing α-Mo vol pct. Also note the dramatic decrease in power-law exponent (78 to 4) for alloy C49 when the temperature is raised from 25 °C to 1300 °C.

is expected for ductile metals, which typically have m values in the range 2 to 4 for the midrange of growth rates.[24]

The ΔK_{TH} thresholds ranged between 5 and 9.5 MPa$\sqrt{m}$ for the five alloys at 25 °C (Figure 4). Specific values for each alloy are given in terms of $K_{max,TH}$, the maximum stress intensity at the fatigue threshold, in Table III. Here, $K_{max,TH}$ was chosen as the most appropriate parameter since the fatigue of brittle materials is generally most influenced by K_{max}, with a lesser dependence on ΔK.[24] Note, both expressions of the fatigue threshold are related, however, *via* the load ratio:

$$\Delta K_{TH} = K_{max,TH}(1-R) \quad [4]$$

At 1300 °C, due to experimental difficulties and limited numbers of samples, data were not collected near the operationally defined fatigue threshold; however, based on extrapolation of the data in Figure 4, the threshold for M34 is expected to be similar to that at 25 °C, whereas data for alloy C49 suggest a decrease in the fatigue threshold at 1300 °C.

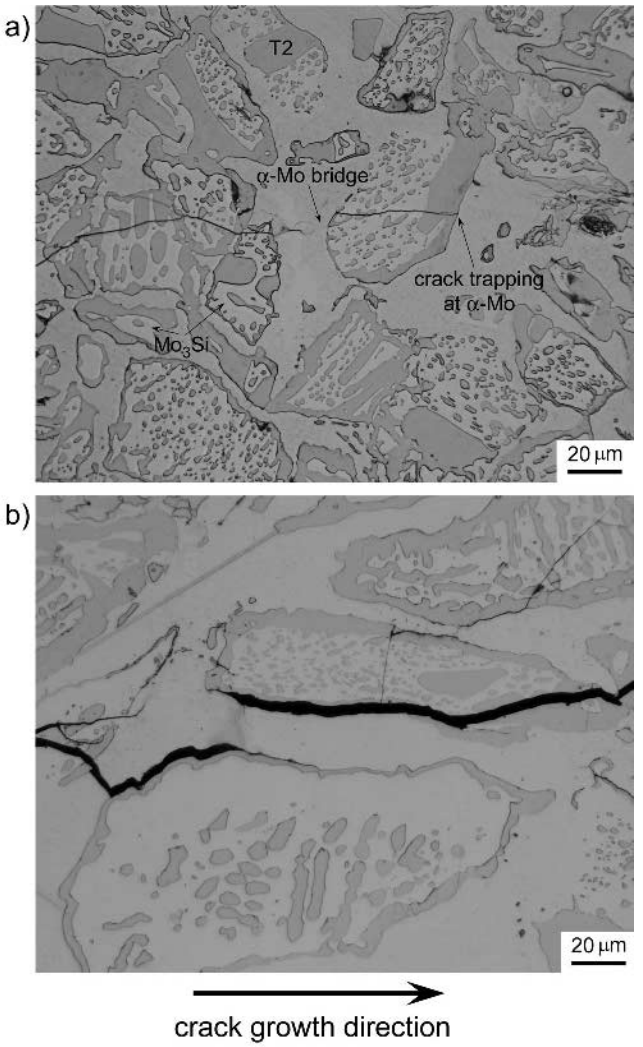

Fig. 5—(*a*) Crack trapping and bridging at the α-Mo phase in alloy M34. The crack locally arrests at the α-Mo phase, leaving α-Mo bridges in the crack wake. (*b*) Crack bridging 3.3 mm behind the crack tip in alloy C46, illustrating how this mechanism can account for the rising R-curve behavior over several millimetres, as seen in Fig. 2. Both specimens were tested at room temperature and etched with Murakami's reagent.

D. *Toughening Mechanisms*

Observations of the crack profiles revealed crack trapping and crack bridging as the primary toughening mechanisms (Figure 5). Crack trapping refers to the local arrest of crack growth at specific microstructural features, in this case, the α-Mo phase (Figure 5(a)). For the "trapped" crack to overcome this barrier, higher applied driving forces are needed, resulting in higher overall toughness for the material. Crack trapping is related to the inherent local resistance to cracking of the material, and can be classified as an intrinsic toughening mechanism that acts to raise the initiation toughness, K_i.[24]

Conversely, rising R-curve behavior, or crack-growth toughness, is indicative of extrinsic toughening, which acts away from the crack tip and develops with crack extension, leading to rising fracture resistance.[24] Crack bridging, which is observed in the present alloys (Figures 3(b) and 5), is one such mechanism, whereby bridges of material span the wake of the crack, resisting crack opening and sustaining some of the applied load that would otherwise contribute to crack advance. Bridges form

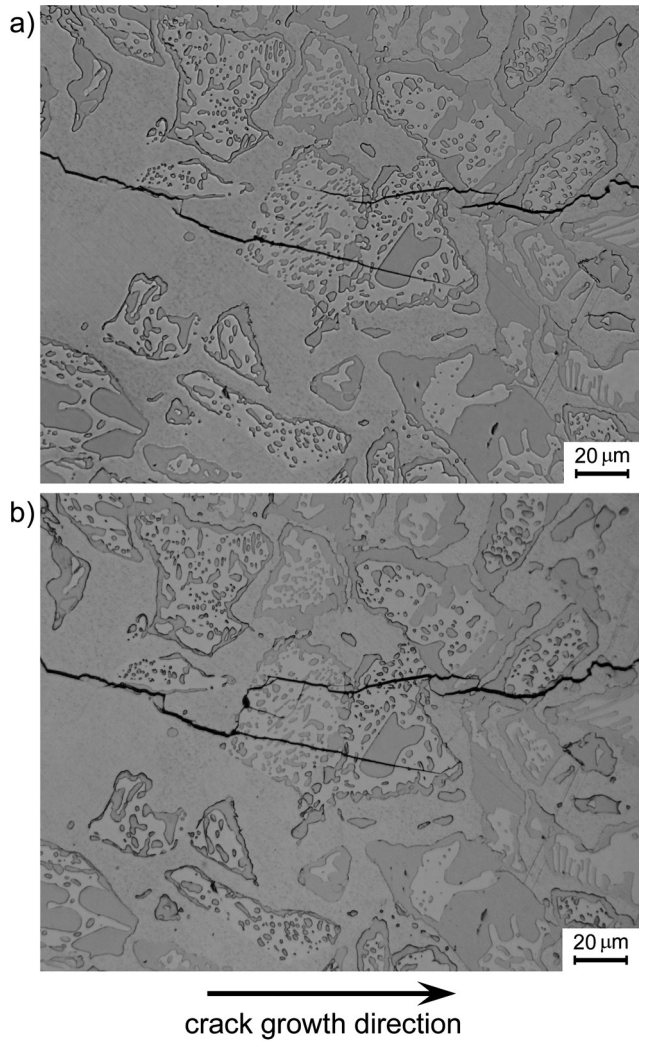

Fig. 6—(*a*) A bridge in alloy M34 located ~400 μm behind the tip of a fatigue crack at room temperature. (*b*) After ~800 μm of additional crack advance, the bridge has been destroyed. The specimen was etched with Murakami's reagent.

during crack extension, leading to the rising toughness with crack growth (*i.e.*, rising R-curve behavior). Although intermetallic bridges were occasionally observed (*e.g.*, Figure 6(a)), most bridges were composed of the α-Mo phase and appeared to result from cracks renucleating in the Mo_3Si and T2 phases ahead of the crack trapping points, *i.e.*, as the crack extended, crack trapping at the α-Mo acted to promote the formation of crack bridges (Figure 5(a)). The existence of bridges persisted over many millimeters behind the crack tip in alloys C17, C46, and C49 (Figure 5(b)), which accounts for the rising toughness seen in these alloys over similar amounts of crack extension (Figure 2). Bridges were observed to degrade during fatigue-crack growth, however, as shown in Figure 6.

The increased fracture resistance at 1300 °C was associated with enhanced crack blunting (Figure 3), while extensive deformation of bridges in the crack wake was also seen (Figure 7). This observed behavior is indicative of the improved α-Mo ductility at elevated temperatures. Conversely, the room-temperature fast fracture surfaces revealed some degree of intergranular failure in the α-Mo phase (Figure 8), which can be attributed to limited ductility of the α-Mo at lower temperatures.

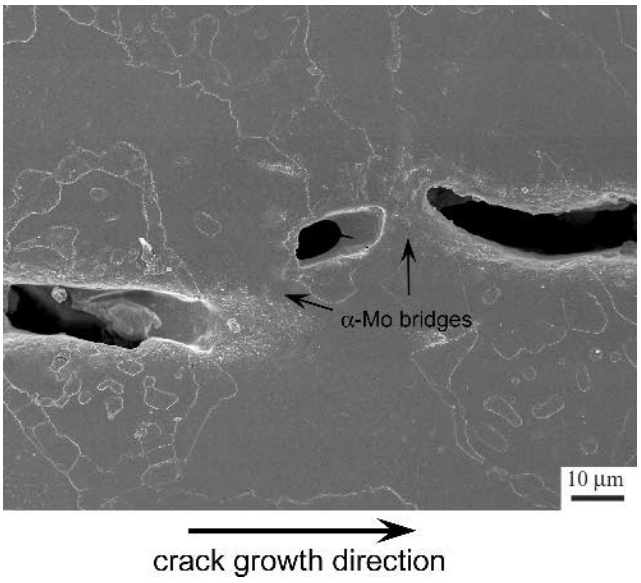

Fig. 7—α-Mo bridges behind the crack tip for alloy M34 after R-curve testing at 1300 °C. Note the large amounts of ductility for the bridges at 1300 °C relative to those tested at room temperature (Fig. 5).

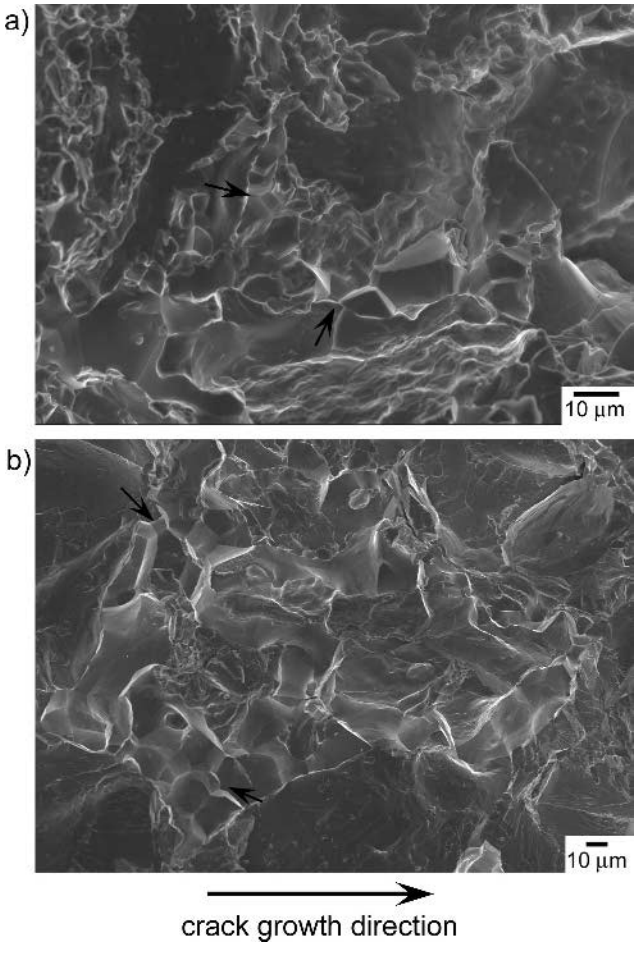

Fig. 8—Room-temperature fast fracture surfaces for alloys (*a*) M34 and (*b*) C49. Flat regions correspond to the cleavage fracture of the intermetallic phases, while arrows point out regions where intergranular failure is apparent in the α-Mo phase.

IV. DISCUSSION

A. *Role of α-Mo Volume Fraction*

It is apparent that the fracture toughness and fatigue-crack growth properties of the α-Mo matrix alloys are progressively improved with increasing α-Mo volume fraction, as shown in Figure 9, where the K_i initiation toughness and $K_{max,TH}$ fatigue threshold values from Table III are included. Also shown in Figure 9 are results on intermetallic matrix Mo-Si-B alloys with similar compositions (22 to 38 vol pct α-Mo),[8,9] which exhibit improved properties with larger α-Mo volume fractions as well. The linear relations on the semilog plot in Figure 9 indicate that K_i and $K_{max,TH}$ increase exponentially (fitted lines) with the α-Mo volume fraction at room temperature for both of these classes of Mo-Si-B materials; however, this trend clearly cannot continue to 100 pct α-Mo as all alloys would have the same toughness at this limit.

Steady-state toughness values, *i.e.*, the peak values from the plateau region of the R-curve, were not measured due to inadvertent specimen failure or limited specimen size (*i.e.*, large-scale bridging conditions), and accordingly are not compared in Figure 9. Based on Figure 2, however, it appears that the crack-growth toughness, or rising part of the R-curve, does benefit from higher levels of α-Mo. This may be concluded from Figure 2(a) when one considers the three alloys C17, C46, and C49, which all were processed from the same coarse starting powder yet had different final α-Mo contents. When comparing their R-curve behavior, it is seen that the alloys with more α-Mo phase have R-curves that rise more steeply. This would imply that peak toughnesses increase with increasing α-Mo by an amount larger than the differences in K_i.

These trends may be understood by considering the salient toughening mechanisms in these alloys, which have been identified as crack trapping and crack bridging. The relatively ductile α-Mo serves as the trapping phase in both the α-Mo and intermetallic matrix alloys, which is fully consistent with the observed increase in crack-initiation toughness with increasing α-Mo volume fraction (Figure 9). Additionally, the potency of crack bridging in the present alloys is aided by increasing the amount of α-Mo. Since most bridging is by the α-Mo phase, as the α-Mo content increases, it is reasoned that more or larger bridges develop as the crack advances, leading to the observed gains in extrinsic toughness.

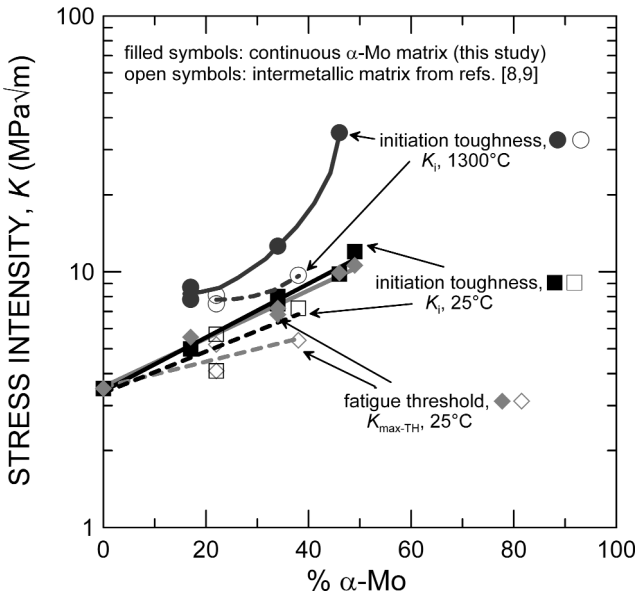

Fig. 9—Comparison of the crack-initiation toughness and fatigue threshold values for the present alloys (Table III) with those for intermetallic matrix alloys that had similar compositions from Refs. 8 and 9; all values are plotted as a function of α-Mo volume percent.

For fatigue-crack growth behavior, room-temperature $K_{max,TH}$ thresholds ($R = 0.1$) also rose with increasing α-Mo content, and were found to be essentially equal to K_i (except at 49 pct α-Mo, where K_i slightly exceeded $K_{max,TH}$) (Figure 9). This suggests that the intrinsic mechanisms for crack advance at ambient temperature are identical under cyclic and monotonic loading for the alloys with α-Mo content $\leq$46 pct. This behavior is common in brittle materials, where high power-law exponents are observed and fatigue-crack growth is typically a result of a cyclic-loading induced degradation in the extrinsic toughening mechanisms.[24] In this case, the degradation occurs by the destruction of bridges due to cyclic loading, as seen in Figure 6 for alloy M34. Even for the 49 pct α-Mo alloy, the power-law exponent, m, remains extremely high, $\sim$78, implying that fatigue-crack advance is still dominated by brittle mechanisms. Indeed, ductile fatigue mechanisms are associated with $m \approx 2$ to 4, while K_i is often an order of magnitude or more larger than $K_{max,TH}$ for ductile metals.[24]

One advantage of the brittle room-temperature fatigue behavior of the present alloys is the high fatigue thresholds relative to traditional (ductile) metallic alloys, where threshold values are typically below 5 MPa$\sqrt{m}$. For high-frequency fatigue applications, where the fatigue-crack growth portion of the lifetime is insignificantly small, high fatigue thresholds are advantageous since higher stresses can be achieved without causing crack advance. However, the accompanying large power-law exponents are not desirable for fatigue applications where a degree of damage tolerance is required, since once a crack starts growing, failure will quickly follow unless the stresses are decaying fast enough to cause crack arrest.

B. *Role of α-Mo Ductility*

Results at 1300 °C reveal the effect of α-Mo ductility on the fracture and fatigue properties of these alloys. Indeed, the main effect of elevated temperature is thought to be the "ductilization" of the α-Mo phase, while the Mo_3Si and T2 phases remain brittle. The initiation toughness values increased by $\sim$65 pct for the C17 and M34 alloys while estimated gains for alloy C46 were on the order of 257 pct, though this latter value is expected to be somewhat elevated due to the plane-stress conditions at 1300 °C (Figure 9). It is interesting to note that, at 1300 °C, the initiation toughness of alloys C17 and M34 exceeded the room-temperature K_i values for alloys with higher α-Mo volume fraction, *e.g.*, 34 and 49 pct, respectively. This implies that less α-Mo would be needed to achieve a given room-temperature toughness provided the ductility is improved. This is important because low α-Mo volume fractions are desirable from the

standpoint of improved oxidation and creep resistance in these alloys.[11,25–28]

Figure 8 shows SEM micrographs of room-temperature fast fracture surfaces for alloys M34 and C49. In these, and indeed the other alloys, there is clear evidence of intergranular fracture of the α-Mo phase, indicative of the low room-temperature ductility of the α-Mo. Intergranular failure in molybdenum is typically associated with impurities such as oxygen, which is known to segregate to and embrittle the grain boundaries.[29] Carbon is thought to offset this effect to some degree, with considerable ductility achieved in unalloyed molybdenum when the C/O ratio is greater than two,[30] although it is not known if similar effects may be expected in the present α-Mo solid solution. Alloys F34 and C17 both had C/O ratios close to unity, while alloy M34 had a high C/O ratio ($\sim$14); the C and O distribution among the phases, however, is unknown (Table I). For alloys C49 and C46, the C concentration was below the detectability limit, making an accurate assessment of the C/O ratio impossible in these alloys. Observations of intergranular failure for alloy M34 (Figure 8(a)), which had a C/O ratio of $\sim$14, suggest that other impurities may play an important role either by direct segregation to the grain boundaries or by affecting the interaction of carbon and oxygen in the α-Mo solid solution, making the critical C/O ratio to achieve adequate ductility different than expected for unalloyed molybdenum. Additionally, Si present in the α-Mo solid solution is known to increase the hardness significantly,[31] which likely reduces the ductility; this suggests that minimizing the Si in the α-Mo phase may be another way to improve the α-Mo ductility. Thus, careful compositional control of the α-Mo phase is expected to be an important factor in improving the fracture resistance of Mo-Si-B alloys.

Although the enhanced α-Mo ductility at higher temperatures has a marked influence on the ductility of the bridges (Figure 7), the crack-growth toughness was relatively unaffected. This may be understood by considering that the increase in ductility of Mo with increasing temperature is accompanied by a decrease in the strength. The enhanced toughness due to ductile-phase bridging may be expressed in terms of the strain-energy release rate, G,* by[32,33,34]

*The strain-energy release rate is an alternative measure of toughness that may be related to the stress intensity for a linear elastic material by $G = K_I^2/E' + K_{II}^2/E' + K_{III}^2/2\mu$, where E' is the appropriate elastic modulus (E in plane stress, $E/(1-\nu^2)$ in plane strain, where ν is Poisson's ratio) and μ is the shear modulus.

$$\Delta G = V_f \sigma_0 t \chi \quad [5]$$

where t is the size of the bridges, σ_0 is the yield strength, V_f is the volume fraction of bridges, and χ is a work of rupture parameter that depends on the strain hardening, ductility, and plastic constraint of the ductile phase. Although rising ductility is beneficial to the bridging contribution through the parameter χ, this will be offset by lower yield strengths at 1300 °C. However, in general, these factors will not completely offset, and there is potential for improving the room-temperature bridging contribution by increasing the ductility, provided the yield strength remains high enough to realize this benefit.

With respect to fatigue, the behavior of alloy C49 changed dramatically at 1300 °C with the power-law exponent falling to 4, characteristic of ductile metals. The lower exponent allows for more damage tolerance in the material, as a considerable amount of the fatigue life will be spent growing an introduced flaw large enough to cause catastrophic failure.

C. *Role of* α*-Mo Matrix*

The present alloys all had continuous α-Mo matrices and their properties are compared in Figure 9 to data from previous studies, which looked at intermetallic matrix Mo-Si-B alloys of similar composition.[8,9] At a given α-Mo volume fraction, the fracture and fatigue properties were improved for the α-Mo matrix materials, particularly at 1300 °C. This behavior is attributed to higher effectiveness of the crack trapping and bridging mechanisms when there is a continuous α-Mo matrix, since the crack cannot avoid the relatively ductile phase. Gains at room temperature were not spectacular; however, these improve with increasing α-Mo volume fraction. Indeed, at 22 pct α-Mo, the benefit to K_i is roughly 0.7 MPa$\sqrt{\text{m}}$, or 15 pct, while at 38 pct α-Mo, the gain is $\sim$1.7 MPa$\sqrt{\text{m}}$, or 26 pct. This effect is enhanced when the α-Mo ductility is higher, achieved here by testing at 1300 °C. For 22 pct α-Mo, the α-Mo matrix alloys have higher K_i values by $\sim$0.8 MPa$\sqrt{\text{m}}$, or 10 pct, while at 38 pct α-Mo, the increase is $\sim$6.1 MPa$\sqrt{\text{m}}$, or 62 pct. Thus, using an α-Mo matrix material is more beneficial at higher α-Mo fractions and ductility. Since the α-Mo matrix is thought to enhance toughness by forcing the crack to interact with the α-Mo phase, it is not surprising that larger amounts and more ductile α-Mo elevates this effect.

D. *Role of Microstructural Scale*

Comparing alloys M34 and F34, which both had 34 pct α-Mo phase with different starting powder sizes, the microstructural size scale appeared to have no effect on the intrinsic toughness or fatigue threshold at room temperature (Table III). There was an effect on the extrinsic toughening (bridging), however, as the R-curve rose higher for alloy M34 (Figure 2). Additionally, crack stability was observed to be improved in alloy M34, with far fewer samples breaking catastrophically during precracking and testing, reflective of easier bridge formation stabilizing crack propagation. This point is illustrated further by the behavior of alloy C17, for which stable rising R-curve behavior was readily achieved over several millimeters despite the low amount (17 pct) of α-Mo phase. Alloy C17 had the largest starting powder size, and thus had a coarser microstructural scale compared to alloys F34 and M34 (Figure 1). Toughening contributions from crack bridging are typically found to be enhanced with coarser microstructures, as seen in a variety of intermetallics, composites, and ceramics.[35,36,37]

E. *Comparing to the Nb-Si System*

The Nb-Si system is another class of refractory metal-silicide–based materials that has received considerable attention for potential high-temperature gas-turbine applications.[38–42] This system presents similar challenges to Mo-Si-B, with the Nb solid solution phase (Nb_{ss}) being ductile, but easily oxidized, and the niobium silicides being very brittle with relatively good oxidation resistance. Fracture

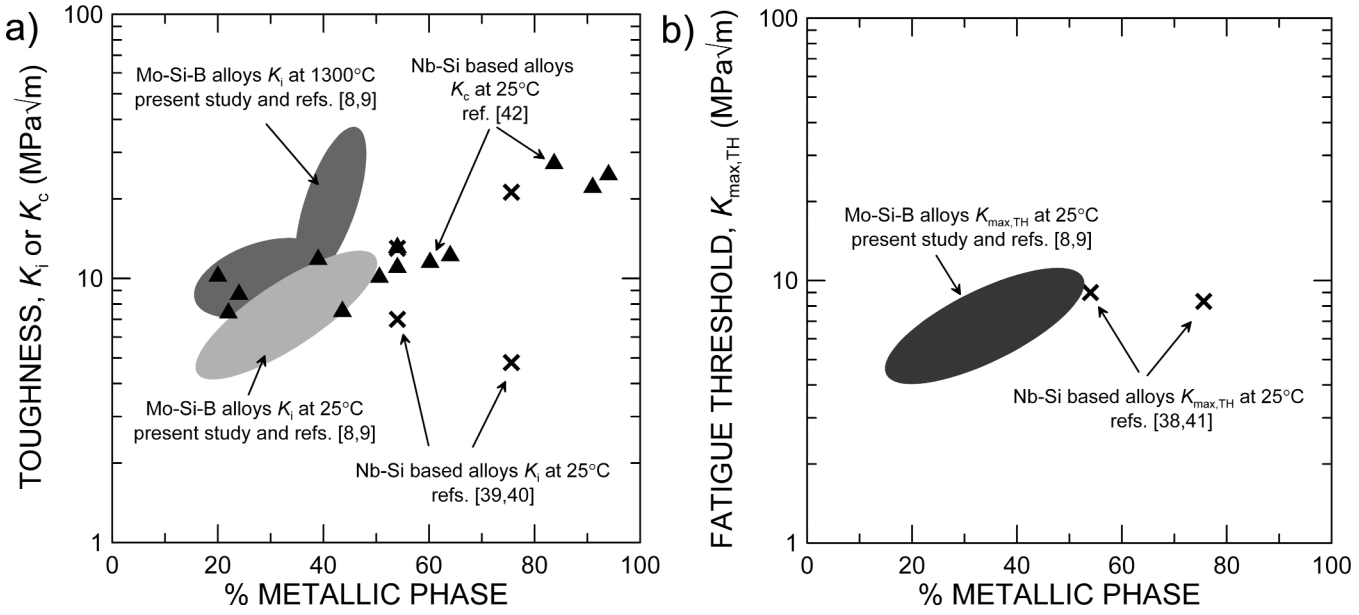

Fig. 10—(*a*) No Crack-initiation toughness and (*b*) fatigue threshold values for Mo-Si-B alloys (present results and References 8 and 9) compared to published results for NB-Si–based materials.[38–42] When assessed as a function of metallic-phase volume percent, the Mo-Si-B alloys appear in line with most Nb-Si alloys in terms of both K_i and $K_{max,TH}$. Note, the toughness values from Ref. 42 were K_c values, which may elevate them relative to K_i, but little R-curve behavior was reported, making these comparisons reasonable.

and fatigue properties have been reported for alloys with 20 to 95 pct metallic Nb_{ss}; these properties are compared to Mo-Si-B alloys from the present study and References 8 and 9 in Figure 10. When the crack-initiation toughness, K_i, is compared at ~50 pct metallic phase, alloy C49 (49 pct α-Mo, $K_i = 12$ MPa$\sqrt{m}$) is similar to the Nb-Ti-Hf-Cr-Al-Si metal and silicide composite (MASC) with 54 pct metallic phase where $K_i = 7$ to 13 MPa$\sqrt{m}$.[39] Furthermore, extrapolation of the initiation toughness data for Mo-Si-B alloys (Figure 10(a)) to higher α-Mo content implies that K_i values should be comparable to the best Nb-Si–based alloys, although such high metallic volume fractions should seriously compromise the oxidation resistance of both systems. Also shown in Figure 10(a) are K_c fracture toughness values (*i.e.*, computed from the peak load at failure) from a study on Nb-Si–based multiphase alloys.[42] The R-curves were not measured in that study since little R-curve behavior was observed; accordingly, these K_c values should approach the initiation toughness, K_i, and be useful for comparison. These alloys, which often contained Laves phases as well as silicides, exhibit slightly superior toughness at low metallic volume percents, but in general appear to fall in line with the present Mo-Si-B alloys as the metallic phase volume percent increases.

One shortcoming of the Mo-Si-B alloys investigated so far is that the R-curves rise much more slowly than some of the Nb-Si systems investigated.[39,40] The latter can achieve toughnesses over 20 MPa$\sqrt{m}$ after only a few hundreds of micrometers of growth[39,40] instead of several millimeters for the present alloys. Enhanced extrinsic toughening is often achieved through microstructural modification (*e.g.*, References 36 and 43), and considering some Nb-Si–based alloys exhibit essentially no R-curve behavior,[42] there is most likely room for improvement in the Mo-Si-B alloys. For example, the Nb-Si–based alloys described in References 39 and 40 had highly anisotropic microstructures achieved by either directional solidification or extrusion processing, with the fracture properties measured transverse to the extrusion or solidification direction. This most likely impacted the R-curve behavior significantly; producing similar microstructures for Mo-Si-B alloys would appear to be a promising approach.

Figure 10(b) compares the room-temperature fatigue thresholds of various Mo-Si-B– and Nb-Si–based alloys; few differences are apparent except for the fact that the Mo-Si-B alloys had lower metal phase content. The reported power-law exponents, however, were as low as $m = 5.3$[41] for some Nb-Si alloys, reflecting the higher metallic phase content and possibly more ductility of the Nb_{ss} phase relative to the α-Mo for the alloys examined. Improving the α-Mo ductility by controlling its composition (*e.g.*, Si content) and impurities (*e.g.*, oxygen) should thus be a high priority for the development of Mo-Si-B alloys.

V. CONCLUSIONS

Based on an experimental investigation into the ambient- to high-temperature fracture toughness and fatigue-crack propagation behavior of five Mo-Si-B alloys, containing Mo_3Si and Mo_5SiB_2 intermetallic phases dispersed within a continuous α-Mo matrix, the following conclusions may be made.

1. The α-Mo matrix Mo-Si-B alloys exhibit fracture and fatigue resistance that is far superior to that of unreinforced silicides; indeed, fracture toughnesses in excess of 20 MPa$\sqrt{m}$ may be achieved for α-Mo volume fractions >45 pct.
2. Crack trapping and crack bridging by the α-Mo phase were found to be the primary toughening mechanisms in these alloys, with the latter leading to rising fracture resistance with crack extension. Furthermore, both of these mechanisms benefited from higher α-Mo volume fractions, leading to improved fracture and fatigue properties.

3. Fracture resistance was improved at 1300 °C, indicating the important role that α-Mo ductility plays in determining the mechanical properties of these alloys. Based on these results, it appears that a given level of fracture resistance may be achieved with lower α-Mo volume fraction by improving α-Mo ductility, a desirable feature since α-Mo compromises the oxidation and creep resistance.
4. Using a continuous α-Mo matrix instead of an intermetallic matrix is also beneficial for the fracture and fatigue properties, with the α-Mo matrix having a larger effect with increasing α-Mo content and ductility.
5. Coarser microstructural size scales also benefit the fracture and fatigue behavior, specifically by aiding bridging and crack stability.
6. When compared as a function of metallic-phase volume percent, the current Mo-Si-B alloys appear to be similar to most Nb-Si–based alloys with respect to their crack-initiation toughness and fatigue threshold values. However, their power-law slopes are much larger than those of niobium silicides, which implies poor tolerance to fatigue crack growth.
7. The success of Mo-Si-B materials for turbine-blade and other high-temperature applications will depend on a compromise between several mechanical properties and the oxidation resistance. The present work defines the role of various microstructural variables in determining the fracture and fatigue properties, and is intended to provide guidelines for the design of superior alloys.

ACKNOWLEDGMENTS

The mechanical property measurements in this work were supported by the Office of Fossil Energy, Advanced Research Materials Program, WBS Element LBNL-2, and the microstructural analysis was supported by the Office of Science, Office of Basic Energy Sciences, Division of Materials Sciences and Engineering, United States Department of Energy, under Contract No. DE-AC03-76SF0098 with the Lawrence Berkeley National Laboratory for ROR and JJK. JHS acknowledges funding of the processing part of this work by the Office of Fossil Energy, Advanced Research Materials (ARM) Program, WBS Element ORNL-2(I), United States Department of Energy, under Contract No. DE-AC05-00OR22725 with Oak Ridge National Laboratory managed by UT–Battelle.

REFERENCES

1. M.J. Donachie: *Superalloys: A Technical Guide*, 2nd ed., ASM, Metals Park, OH, 2002, p. 439.
2. M.K. Meyer, M.J. Kramer, and M. Akinc: *Intermetallics*, 1996, vol. 4, pp. 273-81.
3. M. Akinc, M.K. Meyer, M.J. Kramer, A.J. Thom, J.J. Heubsch, and B. Cook: *Mater. Sci. Eng.*, 1999, vol. A261, pp. 16-23.
4. M.K. Meyer and M. Akinc: *J. Am. Ceram. Soc.*, 1996, vol. 79, pp. 2763-66.
5. M.K. Meyer, A.J. Thom, and M. Akinc: *Intermetallics*, 1999, vol. 7, pp. 153-62.
6. D.M. Berczik: United Technologies Corporation, East Hartford, CT, U.S. Patent 5,595,616, 1997.
7. D.M. Berczik: United Technologies Corporation, East Hartford, CT, U.S. Patent 5,693,156, 1997.
8. H. Choe, D. Chen, J.H. Schneibel, and R.O. Ritchie: *Intermetallics*, 2001, vol. 9, pp. 319-29.
9. H. Choe, J.H. Schneibel, and R.O. Ritchie: *Metall. Mater. Trans. A*, 2003, vol. 34A, pp. 25-239.
10. J.J. Kruzic, J.H. Schneibel, and R.O. Ritchie: *Scripta Mater.*, 2004, vol. 50, pp. 459-64.
11. J.H. Schneibel, R.O. Ritchie, J.J. Kruzic, and P.F. Tortorelli: *Metall. Mater. Trans. A*, 2005, vol. 36A, pp. 525-31.
12. J.H. Schneibel, M.J. Kramer, and D.S. Easton: *Scripta Mater.*, 2002, vol. 46, pp. 217-21.
13. ASTM E561-98: *Annual Book of ASTM Standards*, vol. 03.01, *Metals-Mechanical Testing; Elevated and Low-Temperature Tests; Metallography*, ASTM, West Conshohocken, PA, 2002, pp. 534-46.
14. C.J. Gilbert, J.M. McNaney, R.H. Dauskardt, and R.O. Ritchie: *J. Testing Eval.*, 1994, vol. 22, pp. 117-20.
15. D. Chen, C.J. Gilbert, and R.O. Ritchie: *J. Testing Eval.*, 2000, vol. 28, pp. 236-41.
16. ASTM E647-00: *Annual Book of ASTM Standards*, vol. 03.01, *Metals-Mechanical Testing; Elevated and Low-temperature Tests; Metallography*, ASTM, West Conshohocken, PA, 2002, pp. 595-635.
17. D.M. Dimiduk and J.H. Perepezko: *MRS Bull.*, 2003, vol. 28, pp. 639-45.
18. K.T. Venkateswara Rao, W.O. Soboyejo, and R.O. Ritchie: *Metall. Trans. A*, 1992, vol. 23A, pp. 2249-57.
19. I. Rosales and J.H. Schneibel: *Intermetallics*, 2000, vol. 8, pp. 885-89.
20. C.F. Shih: *J. Mech. Phys. Solids*, 1981, vol. 29, pp. 305-26.
21. A. Buch: *Pure Metals Properties: a Scientific-Technical Handbook*, ASM INTERNATIONAL, Materials Park, OH, 1999, p. 306.
22. K. Ito, K. Ihara, K. Tanaka, M. Fujikura, and M. Yamaguchi: *Intermetallics*, 2001, vol. 9, pp. 591-602.
23. J.G. Swadener, I. Rosales, and J.H. Schneibel: in *High-Temperature Ordered Intermetallic Alloys IX*, J.H. Schneibel, S. Hanada, K.J. Hemker, R.D. Noebe, and G. Sauthoff, eds., Materials Research Society, Warrendale, PA, 2001, pp. N4.2.1-N4.2.6.
24. R.O. Ritchie: *Int. J. Fract.*, 1999, vol. 100, pp. 55-83.
25. J.H. Schneibel, C.T. Liu, D.S. Easton, and C.A. Carmichael: *Mater. Sci. Eng.*, 1999, vol. A261, pp. 78-83.
26. J.H. Schneibel, P.F. Tortorelli, M.J. Kramer, A.J. Thom, J.J. Kruzic, and R.O. Ritchie: in *Defect Properties and Related Phenomena in Intermetallic Alloys*, E.P. George, M.J. Mills, H. Inui, and G. Eggeler, eds., Materials Research Society, Warrendale, PA, 2003, pp. 53-58.
27. V. Supatarawanich, D.R. Johnson, and C.T. Liu: *Mater. Sci. Eng.*, 2003, vol. A344, pp. 328-39.
28. J.H. Schneibel: *Intermetallics*, 2003, vol. 11, pp. 625-32.
29. A. Kumar and B.L. Eyre: *Proc. R. Soc. London A*, 1980, vol. 370, pp. 431-58.
30. J. Wadsworth, T.G. Nieh, and J.J. Stephens: *Scripta Mater.*, 1986, vol. 20, pp. 637-42.
31. N.E. Promisel: *The Science and Technology of Tungsten, Tantalum, Molybdenum, Niobium and Their Alloys*, Pergamon Press, The MacMillan Company, New York, NY, 1964, p. 588.
32. L.S. Sigl, P.A. Mataga, B.J. Dalgleish, R.M. McMeeking, and A.G. Evans: *Acta Metall.*, 1988, vol. 36, pp. 945-53.
33. M.F. Ashby, F.J. Blunt, and M. Bannister: *Acta Metall.*, 1989, vol. 37, pp. 1847-57.
34. B.D. Flinn, M. Rühle, and A.G. Evans: *Acta Metall.*, 1989, vol. 37, pp. 3001-06.
35. D.R. Bloyer, K.T. Venkateswara Rao, and R.O. Ritchie: *Metall. Mater. Trans. A*, 1998, vol. 29A, pp. 2483-96.
36. J.P. Campbell, K.T. Venkateswara Rao, and R.O. Ritchie: *Metall. Mater. Trans. A*, 1999, vol. 30A, pp. 563-77.
37. R.W. Steinbrech, A. Reichl, and W. Schaarwächter: *J. Am. Ceram. Soc.*, 1990, vol. 73, pp. 2009-15.
38. B.P. Bewlay, M.R. Jackson, J.-C. Zhao, P.R. Subramanian, M.G. Mendiratta, and J.J. Lewandowski: *MRS Bull.*, 2003, vol. 29, pp. 646-53.
39. B.P. Bewlay, M.R. Jackson, and H.A. Lipsitt: *Metall. Mater. Trans. A*, 1996, vol. 27A, pp. 3801-08.
40. J.D. Rigney and J.J. Lewandowski: *Metall. Mater. Trans. A*, 1996, vol. 27A, pp. 3292-306.
41. W.A. Zinsser, Jr. and J.J. Lewandowski: *Metall. Mater. Trans. A*, 1998, vol. 29A, pp. 1749-57.
42. K.S. Chan and D.L. Davidson: *Metall. Mater. Trans. A*, 2003, vol. 34A, pp. 1833-49.
43. C.J. Gilbert, J.J. Cao, W.J. Moberly Chan, L.C. De Jonghe, and R.O. Ritchie: *Acta Metall. Mater.*, 1996, vol. 44, pp. 3199-214.